



**HAL**  
open science

## Influence of Solar Wind Variations on the Shapes of Venus' Plasma Boundaries Based on Venus Express Observations

C. Signoles, M. Persson, Y. Futaana, S. Aizawa, N. André, S. Bergman, A. Fedorov, V. Lindwall, N. Martinez, C. Mazelle, et al.

► **To cite this version:**

C. Signoles, M. Persson, Y. Futaana, S. Aizawa, N. André, et al.. Influence of Solar Wind Variations on the Shapes of Venus' Plasma Boundaries Based on Venus Express Observations. *The Astrophysical Journal*, 2023, 954 (1), pp.95. 10.3847/1538-4357/ace7b1 . hal-04263524

**HAL Id: hal-04263524**

<https://hal.science/hal-04263524v1>

Submitted on 29 Oct 2023

**HAL** is a multi-disciplinary open access archive for the deposit and dissemination of scientific research documents, whether they are published or not. The documents may come from teaching and research institutions in France or abroad, or from public or private research centers.





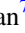



L'archive ouverte pluridisciplinaire **HAL**, est destinée au dépôt et à la diffusion de documents scientifiques de niveau recherche, publiés ou non, émanant des établissements d'enseignement et de recherche français ou étrangers, des laboratoires publics ou privés.



Distributed under a Creative Commons Attribution 4.0 International License



# Influence of Solar Wind Variations on the Shapes of Venus' Plasma Boundaries Based on Venus Express Observations

C. Signoles<sup>1,2</sup>, M. Persson<sup>1,3</sup> , Y. Futaana<sup>4</sup> , S. Aizawa<sup>5,6</sup> , N. André<sup>1</sup> , S. Bergman<sup>7</sup> , A. Fedorov<sup>1</sup> , V. Lindwall<sup>8</sup>,  
N. Martinez<sup>8</sup>, C. Mazelle<sup>1</sup> , S. Rojas Mata<sup>4</sup> , A. Wolff<sup>8</sup>, and T. L. Zhang<sup>9</sup>

<sup>1</sup>IRAP, CNRS-UPS-CNES, Toulouse, France; [moa.persson@irap.omp.eu](mailto:moa.persson@irap.omp.eu)  
<sup>2</sup>Institut Supérieur de l'Aéronautique et de l'Espace, Supaero, Université de Toulouse, Toulouse Cedex, France

<sup>3</sup>Graduate School of Frontier Sciences, The University of Tokyo, Kashiwa, Japan

<sup>4</sup>Swedish Institute of Space Physics, Kiruna, Sweden

<sup>5</sup>ISAS/JAXA, Sagami, Japan

<sup>6</sup>University of Pisa, Pisa, Italy

<sup>7</sup>Department of Earth and Planetary Science, Graduate School of Science, The University of Tokyo, Tokyo, Japan  
<sup>8</sup>University of Technology, Kiruna, Sweden

<sup>9</sup>Space Research Institute Austrian Academy of Sciences, Graz, Austria

Received 2023 March 28; revised 2023 July 6; accepted 2023 July 7; published 2023 August 25

## Abstract

The interaction between the solar wind and Venus creates an induced magnetosphere. The regions of the induced magnetosphere are separated by plasma boundaries, where their shapes and sizes are influenced by variations in the surrounding environment. Investigations of the boundaries and their variability can help us understand the solar wind's effect on Venus and unmagnetized planets in general. In this study, the bow shock and ion composition boundary locations are investigated using, for the first time, the full data set of plasma and magnetic field measurements by Venus Express taken during 2006–2014. The locations of the boundaries are examined with respect to upstream conditions and the solar cycle. We find, in agreement with previous studies using Pioneer Venus Orbiter measurements, that the bow shock location is mostly sensitive to the solar cycle and the dynamic pressure and that it exhibits asymmetries in the terminator plane, depending on the direction of the interplanetary magnetic field. The asymmetries are mainly attributed to the asymmetry in the pickup ion distribution and thus mass loading in the magnetosheath. The ion composition boundary on the dayside is found to decrease in altitude with increasing dynamic pressure during solar maximum (2006–2011), but shows no clear trends during solar minimum (2011–2014) conditions.

*Unified Astronomy Thesaurus concepts:* [Venus \(1763\)](#); [Planetary bow shocks \(1246\)](#); [Plasma physics \(2089\)](#)

## 1. Introduction

Unlike Earth, Venus lacks an intrinsic magnetic field, and thus the solar wind interacts directly with the Venusian atmosphere. The upper atmosphere is ionized by the Sun's extreme ultraviolet (EUV) radiation and forms a conductive ionosphere, in which electric currents flow and generate an induced magnetosphere. This is believed to protect the planet from being completely stripped by the solar wind (Futaana et al. 2017 and references therein). As the supersonic and super-Alfvénic solar wind meets the conductive ionosphere, a bow shock (BS) is formed. As the solar wind plasma passes through the BS, it is slowed, heated, and deflected. Closer to the planetary body, a transition region is formed, upstream of which the magnetosheath plasma dominates, while downstream the planetary plasma dominates. Within this transition region, several different boundaries have been identified and named throughout the years, depending on which parameters are examined or which plasma processes are in focus (e.g., Phillips & McComas 1991; Russell et al. 2006; Holmberg et al. 2019). One important definition concerns the compositional change from energetic solar wind protons and electrons in the magnetosheath to heavy ions of planetary origin. This boundary is commonly named the ion composition boundary

(ICB; Martinecz et al. 2008). Since changes in the shape of these plasma boundaries reflect the nature of the interaction between the shocked solar wind ions and the planetary ion population, knowing which solar wind parameters influence their morphology can help us in the understanding of the interaction between a solar (or stellar) wind and the ionosphere of an unmagnetized planet.

The first mission to verify the conjectures previously made about the Venusian atmosphere's sensitivity to the upstream environment was the Pioneer Venus Orbiter (PVO), which orbited Venus between 1978 and 1992, covering a full solar cycle (Colin 1980; Russell 1992). The key findings of this mission include the BS distance from Venus increasing with an increase in the solar EUV radiation flux, decreasing with the magnetosonic and Alfvén Mach numbers, and changing its shape with respect to the interplanetary magnetic field (IMF) orientation (Tatallyay et al. 1983; Russell et al. 1988; Zhang et al. 1990; Phillips & McComas 1991; Russell et al. 2006). However, orbital biases limited PVO's investigation of the BS shape to regions near the terminator plane and the distant tail region and of the ICB to periods of solar minimum activity (Slavin et al. 1980; Russell et al. 2006).

The more recent Venus Express (VEX) mission (Svedhem 2007), which operated between 2006 and 2014, provided more information about the Venus–solar wind interaction. With a periapsis close to the North Pole, and a highly elliptical orbit, VEX crossed the BS at almost all solar zenith angles (SZAs) from near the subsolar point to near  $-4 R_V$  (Venus radii, 6052 km)



Original content from this work may be used under the terms of the [Creative Commons Attribution 4.0 licence](#). Any further distribution of this work must maintain attribution to the author(s) and the title of the work, journal citation and DOI.

downstream on the nightside. In addition, the periaapsis altitude was nominally located at  $\sim 250$  km, which allowed the investigation of the ICB altitude. Previous studies using the VEX data set have mainly incorporated the first few years of measurements, which occurred during solar minimum conditions (around 2006–2010). These studies found that the BS distance from Venus is insensitive to solar wind dynamic pressure changes and that it is closer to the planet during the solar minimum conditions during the VEX era compared to the solar maximum conditions during the PVO era (Martinecz et al. 2008, 2009) and a short period of solar maximum measurements by VEX in 2011–2012 (Shan et al. 2015).

In this study, we show the first investigation of the Venusian BS and ICB using the full data set collected by the VEX mission during 2006–2014, which included more than 3000 orbits. The goal is to use this large statistical database to assess and confirm the influences of the upstream parameters on the shapes and locations of these boundaries. We will also compare with the findings of the previous studies using PVO measurements and smaller data sets of VEX measurements. In Section 2, we present the data set and the methods used to investigate the boundary locations. In Section 2.1, we present the dependencies of the boundary shapes on upstream parameters. In Section 2.2, we discuss the results and compare them to previous studies, and in the last section we end with a summary of the conclusions.

## 2. Materials and Methods

### 2.1. Instrumentation and Data Sets

To determine the locations of the boundaries, we use combined plasma and magnetic field measurements from the VEX mission. The Ion Mass Analyser (IMA) and Electron Spectrometer (ELS), both part of the Analyser of Space Plasma and Energetic Neutral Atoms (ASPERA-4) instrument package (Barabash et al. 2007), provided the plasma data, and the magnetometer (MAG) instrument (Zhang et al. 2007) provided the magnetic field data.

IMA is a spherical top-hat electrostatic analyzer, which measures ions in the energy range 0.01–36 keV, with an energy resolution of  $dE/E = 7\%$  and a total field of view (FoV) of  $90^\circ \times 360^\circ$ , composed of 16 elevation  $\times$  16 azimuth pixels of  $5.6^\circ \times 22.5^\circ$  each, and can separate the heavier from the lighter ion species with a set of permanent magnets. IMA measures the 3D velocity distribution function with a cadence of 192 s. The ELS sensor measures electrons in the energy range of 0.01–15 keV, with a total FoV of  $5^\circ \times 360^\circ$ , separated into 16 azimuthal sectors, with a cadence of 4 s. The MAG instrument is a fluxgate magnetometer that measures the three magnetic field vector components with a resolution up to 32 Hz. Here we used a time resolution of 4 s for the magnetic field vector measurements.

### 2.2. Boundary Identification

An example of the plasma and magnetic field data around the pericenter for one VEX orbit is presented in Figure 1. The boundary crossings can confidently be determined by combining the available plasma and magnetic field measurements. The boundary crossings were identified by eye inspection, where an example is included in Figure 1. During an inbound orbit, the BS crossing is characterized by a sharp increase in the magnetic field magnitude, as well as an increase in the energetic ion and

electron counts and widths of their energy distributions (i.e., the temperatures). The time resolution of both the MAG and ELS data is 4 s, which means that the boundary can be identified with the same resolution. An error of 4 s at the VEX maximum speed of  $\sim 8$  km s $^{-1}$  is approximately 32 km, which is equal to or smaller than the typical width of the BS (e.g., Newbury et al. 1998; Hobara et al. 2010). The ICB is identified from the IMA and ELS measurements by the decrease in magnetosheath protons and electrons and the increase in lower-energy planetary heavy ions. Typically, ELS provided the best indication of the boundary crossing, which provides a similar error as for the BS. However, when the ELS measurements were unclear, the IMA measurements were used. The maximum error for using the IMA measurements is estimated as half of the IMA time resolution of 192 s, which provides a maximum error of  $\sim 750$  km.

In some cases, for example when the boundary crossing was made at a large angle to the boundary normal, or during a quasi-parallel BS crossing, the changes in the measurements appear more gradually, leading to a difficulty in identifying a clear crossing location. To avoid ambiguities, crossings with a time uncertainty larger than half an IMA sweep (96 s) were omitted from this study. This leads to both a bias toward quasi-perpendicular BS crossings and dayside ICB crossings. Therefore, the ICB analysis is restricted to the dayside. From over 6000 boundary crossings over the entire VEX mission, we have identified a total of 5193 BS crossings and 2679 ICB crossings.

### 2.3. Boundary Shapes and Locations

To take into account the solar wind aberration due to the orbital motion of Venus, the boundary crossing positions are calculated in the aberrated Venus Solar Orbital (VSO) coordinate system ( $X'$ ,  $Y'$ ,  $Z'$ ). From the VSO coordinate system ( $X$  points from Venus' center toward the Sun,  $Y$  points in the Venus anti-orbital direction, and  $Z$  completes the right-hand system), a rotation toward the  $Y$ -axis with a constant aberration angle about the  $Z$ -axis was applied to obtain the aberrated VSO coordinates. As a solar wind velocity is not available for every boundary crossing, an average aberration angle of  $5^\circ$  is employed, similarly to Martinecz et al. (2009). Evaluating the aberration angle from the available solar wind velocities shows that it may vary by a standard deviation of  $\pm 1^\circ$  from the average. A  $1^\circ$  difference on the boundary locations in the aberrated coordinate system is generally less than about 100 km. The aberrated VSO coordinates are employed throughout this paper unless stated otherwise.

To fit the BS shape, we use the technique described by Slavin et al. (1980), also employed by Martinecz et al. (2008), which assumes a cylindrical symmetry around the  $X'$ -axis. The BS crossings are least-squares fitted with a conic section curve

$$d = \frac{L}{1 + \varepsilon \cos \theta}, \quad (1)$$

where  $d = \sqrt{(X' - x_0)^2 + Y'^2 + Z'^2}$  and  $\cos \theta = \frac{X' - x_0}{d}$  are the polar coordinates measured with respect to a focus location at  $(x_0, 0, 0)$ .  $L$  is the semi-latus rectum and  $\varepsilon$  is the conic's eccentricity. The fitting procedure applied to the full data set gives the smallest rms deviation normal to the curve for a focus at  $x_0 = 0.688 R_V$ , which we keep fixed throughout the rest of the study.

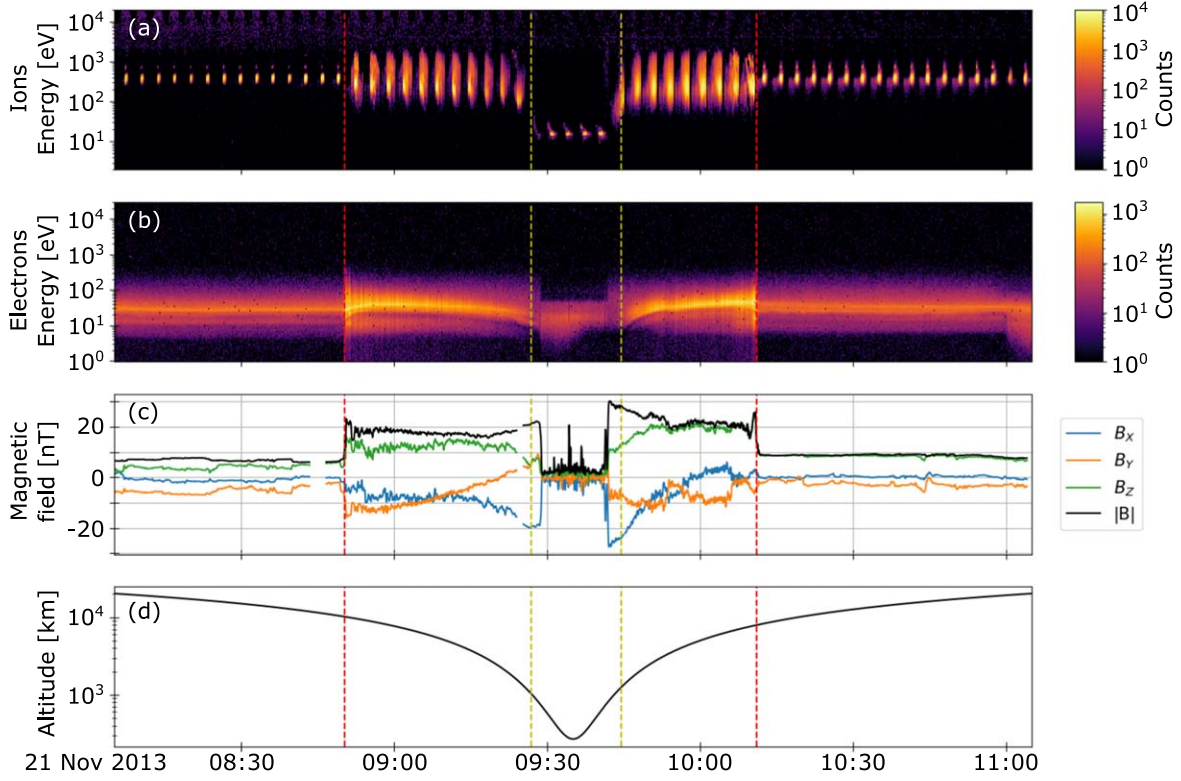


**Figure 1.** Ions, electrons, and magnetic field measurements recorded on 2013 November 21, near the pericenter. Panels (a) and (b) show the energy–time spectrograms of ASPERA-4 ions (IMA) and electrons (ELS), respectively; panel (c) shows the MAG magnetic field measurements in the VSO coordinates; and panel (d) shows the VEX altitude above the Venus radius (i.e.,  $R_V = 6052$  km). The dashed vertical lines show the identified boundary crossing locations: red for the BS and yellow for the ICB.

Following the method of Martinecz et al. (2008), we fit the dayside ICB crossings with a circle of radius  $d_c$ , and so end up with a simple altitude dependence to the upstream conditions.

#### 2.4. Upstream Conditions

To establish the relation between the boundary locations and the upstream conditions, we need to find the upstream condition that was present during each identified boundary crossing. In this study, we focused on the solar wind dynamic pressure, the IMF strength and orientation, and the solar cycle. Due to the lack of an upstream monitor, the upstream conditions are calculated from the measurements made by VEX upstream of the BS, and are assumed to be stable for the boundary crossings of that orbit. Therefore, each orbit crossing is only considered if the upstream conditions are stable over a defined time range outside of and close to the BS.

The solar wind conditions are computed from the proton moments of the ASPERA-4/IMA measurements (see Fedorov et al. 2011). We define stable conditions for the solar wind as when the density does not vary by more than  $5 \text{ cm}^{-3}$  and the velocity does not vary by more than  $35 \text{ km s}^{-1}$  over a 40 min time range, located at a distance about 20 minutes outside of the identified BS crossing. The solar wind dynamic pressure  $P_{\text{dyn}}$  is then derived from the average stable solar wind density and velocity as  $P_{\text{dyn}} = \frac{m_p n_{\text{sw}} v_{\text{sw}}^2}{2}$ , where  $m_p$  is the proton mass.

The IMF conditions are calculated from the magnetic field measurements by MAG. The IMF conditions are selected by adapting the steady IMF criteria used by Rong et al. (2014). First, an average IMF vector is calculated over a 20 minutes interval, located 20 minutes outside of the identified BS

crossing, for both the inbound ( $\vec{B}_i$ ) and outbound ( $\vec{B}_o$ ) BS crossings. The steady IMF criteria are fulfilled if  $\frac{2 \|\vec{B}_o\| - \|\vec{B}_i\|}{(\|\vec{B}_o\| + \|\vec{B}_i\|)} < 0.2$  and when there is not a significant rotation between the inbound and outbound vectors. The steady IMF vector  $\vec{B}$  is then derived as the average between the inbound and outbound vectors. From  $\vec{B}$ , the cone angle  $\cos \varphi = \frac{|B_x|}{B}$  and clock angle  $\tan \theta = \frac{B_y}{B_z}$ , where  $B$  is the magnitude, are derived. For the crossings with both a steady solar wind and IMF magnitude, the Alfvén Mach number can be derived as  $M_a = \frac{v_{\text{sw}}}{v_a}$ , where  $v_a = \frac{B}{\sqrt{\mu_0 m_p n_{\text{sw}}}}$  is the Alfvén speed. For the angle between the inbound and outbound vectors, we need to take into account how many boundary crossings we can use after employing the criteria. A stricter angle gives less crossings to use but a more reliable result, as there is a lower uncertainty on the actual angle during the boundary crossing. Therefore, we employed two different criteria for the angle, depending on the parameter investigated. For parameters related to the relative angle between the BS normal and the IMF (i.e., if the BS is quasi-parallel or quasi-perpendicular, see Figure 4; or the asymmetry of the BS in the terminator plane, see Figure 6), the angle is set to  $< 45^\circ$ , while for parameters related only to the magnitude of the magnetic field (i.e., IMF magnitude or Alfvén Mach number, see Figures 2, 5, and 8), the angle is set to  $< 90^\circ$ . A comparison of the relaxed and strict angle criteria on the parameters related to only the magnitude of the IMF shows no significant differences in the results (not shown), which proves that the relaxed criteria can be used for these parameters.



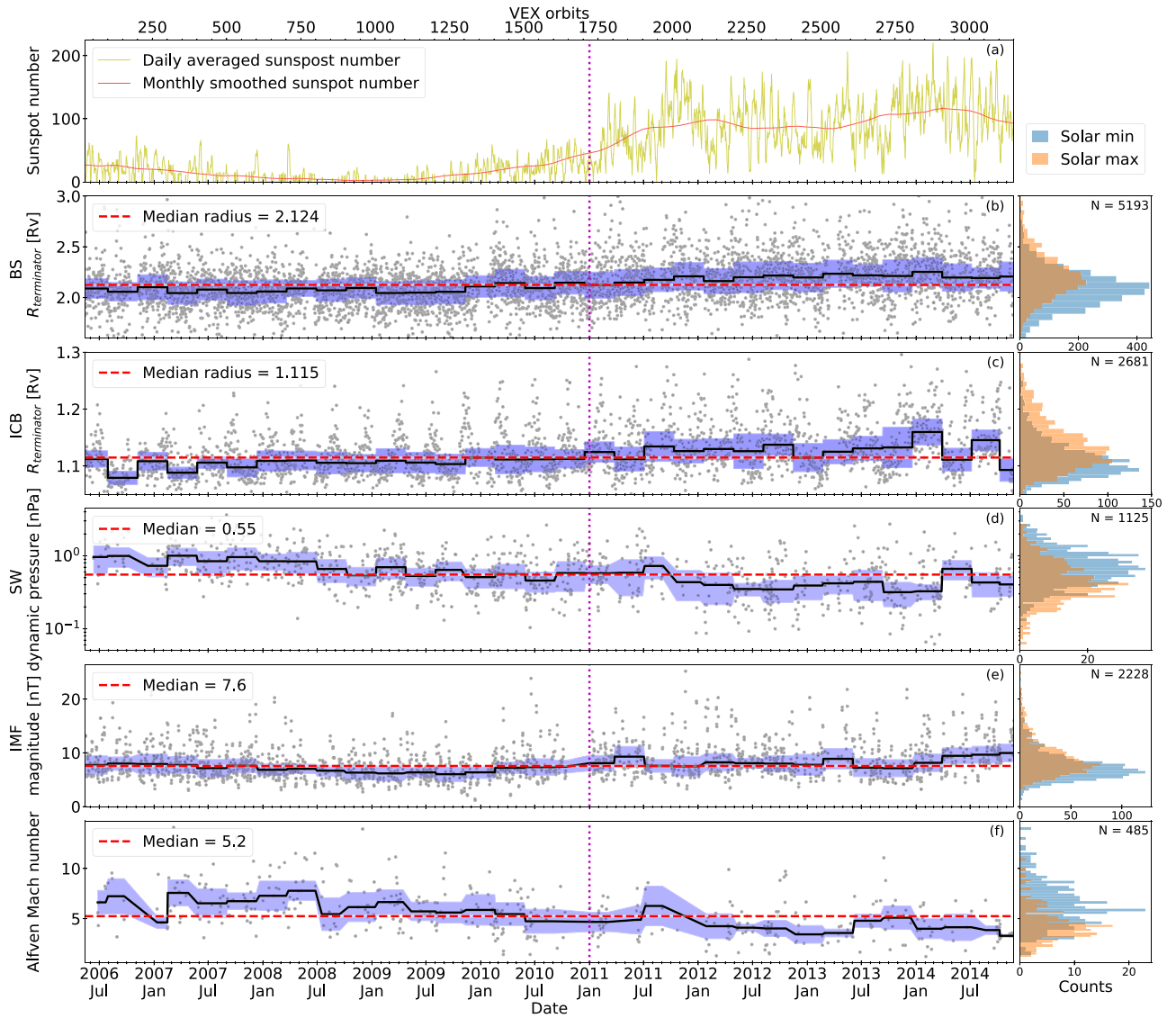


**Figure 2.** Time series of upstream parameters and BS and ICB extrapolated terminator distances over the VEX mission. The corresponding orbit number is shown at the top of the figure. (a) Daily averaged (yellow) and monthly smoothed (red) SSN values. The vertical dotted pink line spanning the whole figure marks the separation between periods of low and high solar activity, on 2011 January 1 (VEX orbit 1716). (b) Extrapolated BS radius (using method II; see Section 2.5). (c) Extrapolated ICB radius at the terminator (see Section 2.5). (d) Measured dynamic pressure of the solar wind. (e) Measured IMF magnitude. (f) Measured Alfvén Mach number, as used in this study. The black lines in (b) and (c) show the trend of the median radius over intervals 100 days wide; the dashed red line represents the general median; and the blue envelope provides the 25th and 75th quartile. A histogram of the values at solar minimum and maximum for each panel is plotted to the right of each time series.

The level of solar activity is estimated using sunspot number (SSN) data, which can be used as a proxy for the solar EUV flux, due to their strong correlation (see, e.g., Russell et al. 1988). The SSN data were retrieved from <https://www.sidc.be/silso/datafiles>. We separate periods of low and high solar activity at the apparent shift from low to high SSN at 2011 January 1.

An overview of the SSN, solar wind dynamic pressure, IMF magnitude, and Alfvén Mach number data used in this study, and the number of orbits used after each respective condition is applied, is displayed in Figure 2.

### 2.5. Boundary Fitting Procedure

In addition to the fitting parameters  $L$  and  $\varepsilon$  (Section 2.3), the boundary shape dependence on the upstream conditions is assessed by the boundary distance in the terminator plane. The

terminator plane represents, to a first order, the plane where the solar wind can interact with the planetary ionosphere and transfer energy; the cross section of the boundaries at the terminator thus defines the size of the solar wind–ionosphere interaction region (Ramstad et al. 2017a, 2017b; Persson et al. 2021).

To retrieve the boundary distance in the terminator plane, we employed two different methods. (I) Calculate the distance at the terminator plane directly from the fitted parametric curve (Section 2.3); or (II) calculate the distance at the terminator plane from a single measurement using the fitted parametric curve, and then average the distance.

In this study, fitting method I was generally used for the BS if a large enough set of boundary crossings was identified with reliable upstream conditions. Method I is preferred over method II as the latter method only allows the use of one fitting parameter, which we chose to be the semi-latus rectum

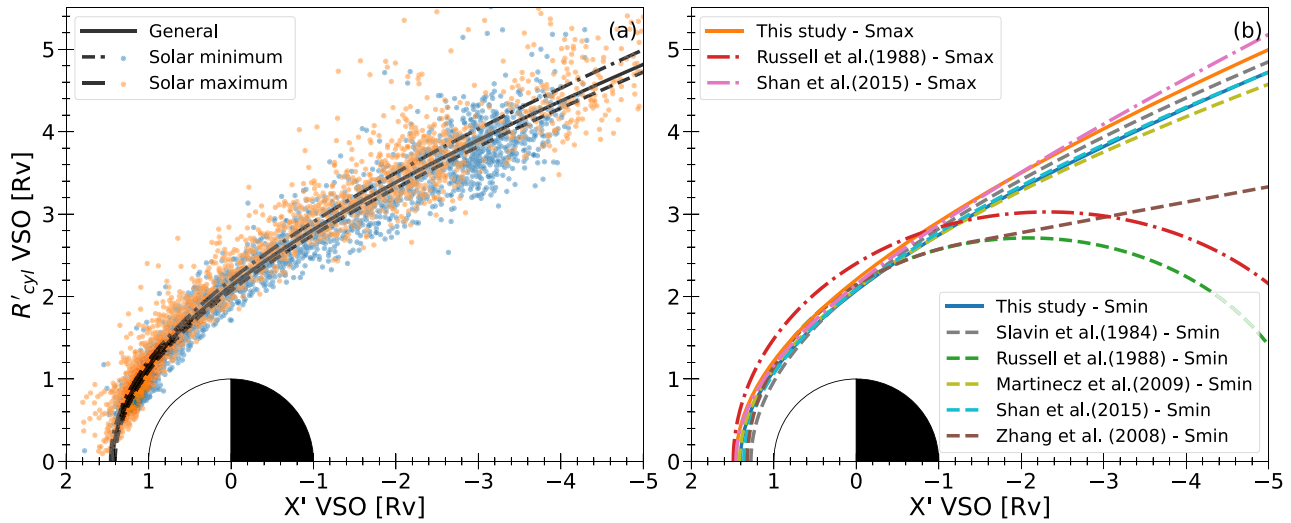


**Figure 3.** BS fits and comparison with other BS models. (a) BS crossings and least-squares fits in aberrated axisymmetric VSO coordinates, at solar minimum (blue dots, dashed black line) and solar maximum (orange dots, dashed-dotted black line). The solid black line is the fitted curve for all crossings. (b) BS fit comparison with other models at solar minimum (Smin) and solar maximum (Smax).

**Table 1**

Summary Table of the BS Fitted Parameters from Previous Studies at Venus for (a) Solar Minimum and (b) Solar Maximum

(a) Solar Minimum Model	Mission	Instrument	Number of Crossings	L (R <sub>V</sub> )	Epsilon	x <sub>0</sub> (R <sub>V</sub> )	R <sub>T</sub> (R <sub>V</sub> )	R <sub>SS</sub> (R <sub>V</sub> )
This study	VEX	ELS, IMA, MAG	2911	1.466	1.042	0.688 <sup>a</sup> (5193)	2.072	1.406
Martinecz et al. (2009)	VEX	ELS	(2006-05-14–2007-12-31)	1.515	1.018	0.664	2.088	1.415
Russell et al. (1988)	PVO	MAG	107	2.15	0.609 <sup>a</sup> (1881)	0 <sup>a</sup>	2.15	(1.34)
Shan et al. (2015)	VEX	MAG	454	1.557	1.03	0.596	2.087	1.363
Slavin et al. (1980)	Mixed <sup>b</sup>	MAG	~66	1.68	1.03	0.45	2.10	1.28
(Zhang 2008) <sup>c</sup>	VEX	MAG	147	2.14	0.621	0 <sup>a</sup>	2.14	1.32
(b) Solar Maximum Model	Mission	Instrument	Number of Crossings	L [R <sub>V</sub> ]	Epsilon	x <sub>0</sub> [R <sub>V</sub> ]	R <sub>T</sub> [R <sub>V</sub> ]	R <sub>SS</sub> [R <sub>V</sub> ]
This study	VEX	ELS, IMA, MAG	2282	1.586	1.052	0.688 <sup>a</sup> (5193)	2.205	1.461
Russell et al. (1988)	PVO	MAG	108	2.4	0.609 <sup>a</sup> (1881)	0 <sup>a</sup>	2.40	(1.49)
Shan et al. (2015)	VEX	MAG	335	1.433	1.095	0.775	2.146	1.459

**Notes.** Note that “MAG” here means “magnetometer” and refers to a different instrument for each mission.  $R_T$  and  $R_{SS}$  are the radii at the terminator and subsolar points, respectively. The values between parentheses indicate a higher uncertainty in the computed number due to a lack of data near the subsolar point in the used data set. If the number of crossings is not specified in the respective study, the measurement period is given in parentheses.

<sup>a</sup> Fixed parameter, typically determined from fitting to all boundaries first; if so, the number of orbits used is shown in parentheses.

<sup>b</sup> Crossings from the Mariner 4 and 10 and Venera 6, 9, and 10 flybys.

<sup>c</sup> Fitted to a conic for  $SZA \leq 117^\circ$  and to a Mach cone of  $10^{\circ}5$  for  $SZA > 117^\circ$ .

$L$ , and thus we used a fixed eccentricity  $\varepsilon$  determined from the fitting of all BS crossings using method I. A comparison of the two methods shows that they generally provide similar results, but method II shows less pronounced trends of the boundary radius variations with respect to each upstream condition. Therefore, method I was used for all boundary shape fittings, except for investigating the effect from the Alfvén Mach number, where there are only 485 crossings that fulfill both the steady solar wind and IMF criteria simultaneously. As a result, the number of crossings within each bin is too small to make a reliable fit. From the fit to each separate boundary crossing (method II), the boundary crossings were extrapolated to the terminator plane using  $R_T = \sqrt{L^2 + 2L\varepsilon x_0 + (\varepsilon^2 - 1)x_0^2}$ . We then analyze only the evolution of the median estimated terminator distance within each Alfvén Mach number bin.

For the ICB, a slightly simpler process is employed. As the dayside ICB can be estimated as a circle, we use the distance to the center of Venus as an approximation of the radius at the terminator.

To evaluate the validity of our assumptions, we evaluate the terminator distance for each BS and ICB boundary crossing using method II and compare the global median value to the value obtained from making a fit to all the boundaries at the same time using method I. Figures 2(b) and (c), inspired by Hall et al. (2019), present the BS and ICB estimated radius at the terminator as it evolved over the VEX mission. From this figure, we confirm that the general radius at the terminator from fitting method I is within the uncertainty range of the individual values obtained from each boundary crossing using method II:  $R_T = 2.128 \pm 0.004 R_V$  for the BS and  $R_T = 1.115 \pm 0.023 R_V$  for the ICB.

### 3. Results

#### 3.1. BS Dependencies

Figure 3 displays the BS crossings and the derived fitted curves during solar minimum and solar maximum, with the averaged fitted curve over the full mission (Figure 3(a)) and a comparison with previous studies of the average BS position

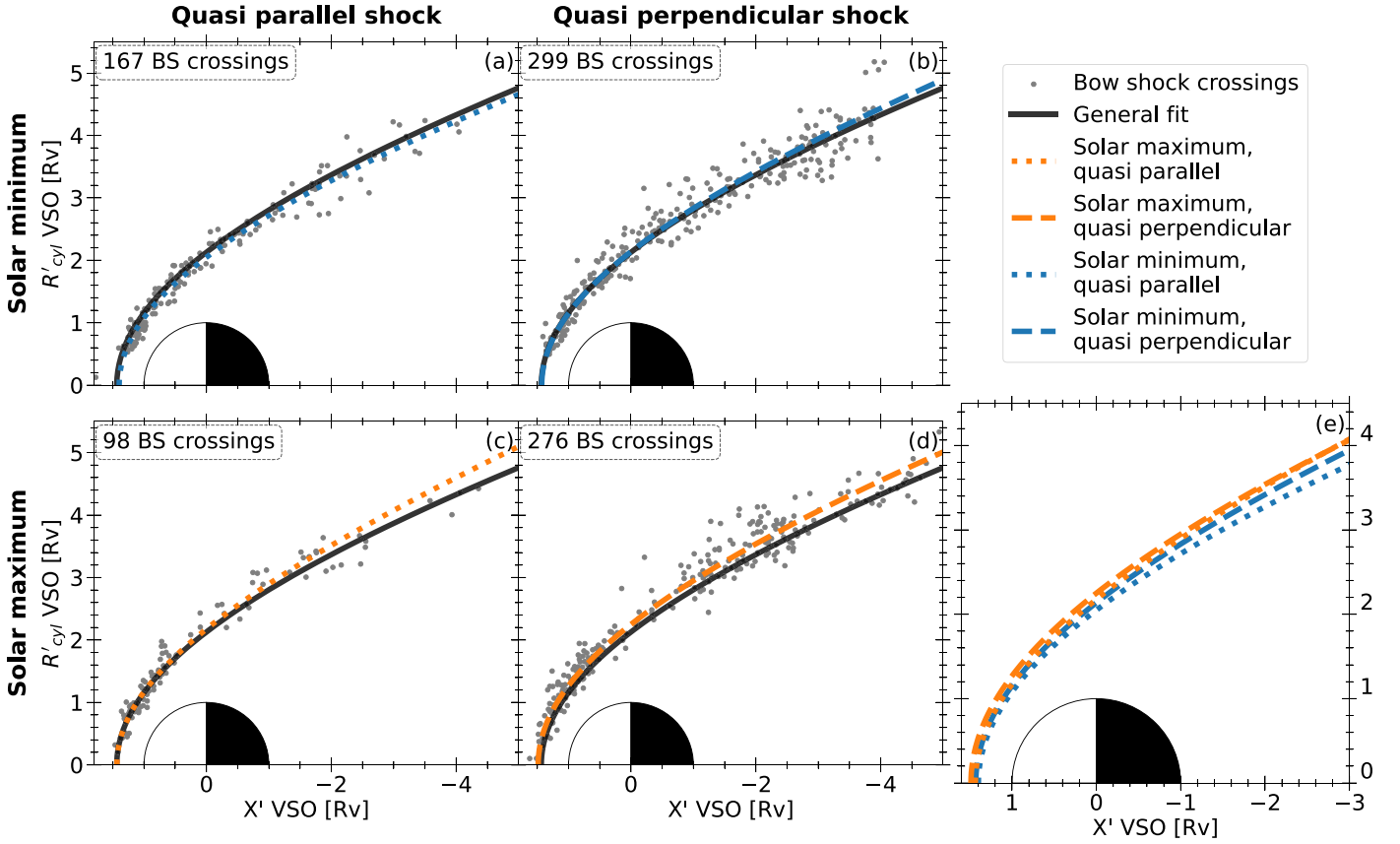


**Figure 4.** Dependence of the BS shape on both solar activity and shock geometry. BS crossings (gray dots) at solar minimum (panels (a) and (b), blue lines) or maximum (panels (c) and (d), orange lines) and for the  $q_{\parallel}$  (panels (a) and (c), dashed lines) or  $q_{\perp}$  (panels (b) and (d), dashed-dotted lines) shock crossings, with the corresponding and general fitted lines (colored and black lines, respectively). A comparison between all fits is shown in panel (e).

and shape (Figure 3(b)). Information about the mission and instruments used to determine the crossing positions and the fitted parameters for each study is provided in Table 1. Note that the large deviations in Russell et al. (1988) and Zhang et al. (2008) in the far tail region presumably come from neglecting the offset of the cone focus ( $x_0$ ) and using a limited range of crossings in the  $X_{\text{VSO}}$ -direction (mainly near the terminator) when fitting the boundary shapes.

The results show that the BS is expanded during solar maximum compared to solar minimum. Moreover, the location of the BS is more variable at solar maximum, which is consistent with the higher SSN fluctuations observed during this period (see Figure 2).

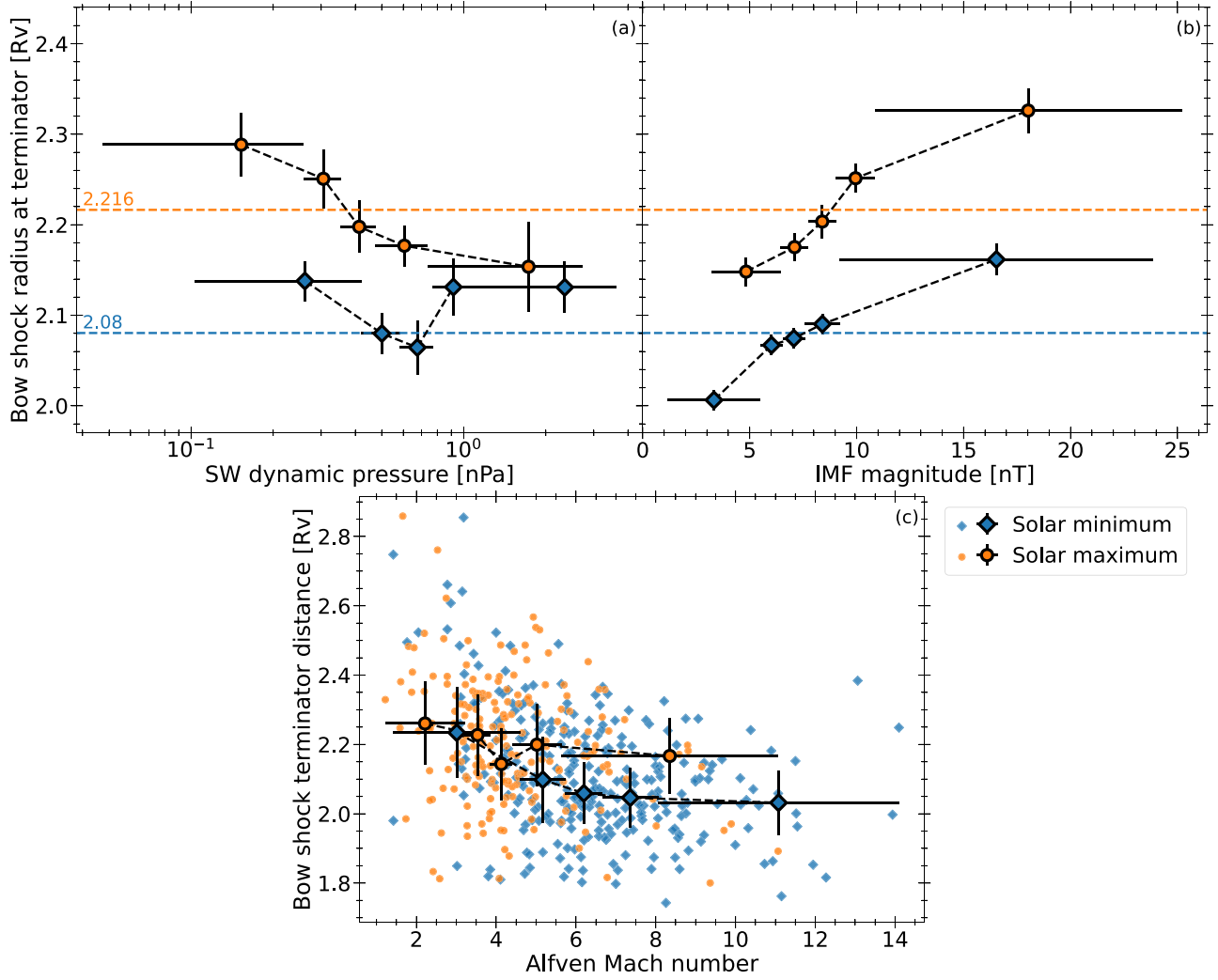
Another driver of the BS position that we investigated is the IMF orientation relative to the shock surface, which defines the geometry of the shock in the region of the crossing. The shocks are divided into quasi-perpendicular  $q_{\parallel}$  and quasi-parallel shocks  $q_{\perp}$ , where the angle between the IMF and the shock normal  $\theta_{\text{Bn}}$  is  $>45^\circ$  and  $<45^\circ$ , respectively. The normal to the BS surface is estimated through geometrical considerations from the average fitted BS shape. Over the 968 crossings where the geometry of the shock is established, the majority (669) are  $q_{\perp}$  shocks, as these show a sharper crossing with generally less wave activity, which makes it easier to determine a more exact crossing time.

Figure 4 illustrates the effects of both solar activity and shock geometry on the BS position, where we see the  $q_{\parallel}$  BS crossings are generally closer to the planet than the  $q_{\perp}$  ones. Focusing on the radius at the terminator, we find a  $0.12 R_V$ , or

$\sim 6\%$ , increase between low- and high-solar-activity conditions and a  $0.08 R_V$ , or  $\sim 4\%$ , increase between  $q_{\parallel}$  and  $q_{\perp}$  shock crossings. We could therefore contemplate taking both solar activity and shock geometry conditions into account before binning the crossing locations according to another upstream parameter, but the remaining number of crossings within each bin would be too few to guarantee a reliable fit. Additionally, and unlike the solar cycle, we find that the shock geometry is not correlated to any upstream parameters other than the IMF orientation. Thus, for these parameters, we can forgo taking the geometry of the shock crossings into account without risking introducing a bias in the results.

Figure 5 illustrates the dependence of the BS radius at the terminator on the solar wind dynamic pressure (panel (a)), IMF strength (panel (b)), and the Alfvén Mach number (panel (c)). At solar minimum,  $R_T$  is slightly lower for intermediate  $P_{\text{dyn}}$  compared to the higher and lower  $P_{\text{dyn}}$ , while at solar maximum, the BS shrinks for higher  $P_{\text{dyn}}$ . On the other hand, the BS expands with higher IMF magnitude for both solar minimum and maximum (Figure 5(b)). Therefore, at solar maximum,  $P_{\text{dyn}}$  and  $B$  have opposite effects on the size of the BS.

Figure 5(c) indicates a negative correlation between the median  $R_T$  and  $M_a$  during solar minimum. During solar maximum, the individual crossings are highly scattered for small  $M_a$  values, introducing large error bars, and the  $R_T$  median is constant for intermediate  $M_a$ . Therefore, the results indicate that the BS position is independent of the Mach number at solar maximum. The Alfvén Mach number can also



**Figure 5.** BS radius at the terminator and its dependence on upstream parameters for solar minimum and solar maximum. Dependence on (a) the solar wind dynamic pressure and (b) the IMF magnitude. The vertical error bars are obtained from the standard errors on the fitted parameters propagated to the radius at the terminator. The horizontal dotted lines are the radius at the terminator value for the solar minimum (blue) and solar maximum (orange) BS fits. (c) Dependence on the Alfvén Mach number: BS crossings (blue for solar minimum and orange for solar maximum) extrapolated to the terminator plane (see Section 2.5). The blue diamonds (solar minimum) and orange circles (solar maximum) represent the median values over the Alfvén Mach number bins, and the vertical error bars show the median absolute deviation. In each plot, the horizontal error bars indicate the bin sizes.

be expressed as  $M_a \propto \frac{\sqrt{P_{\text{dyn}}}}{B}$ , which means that it is connected to the dependencies from both  $P_{\text{dyn}}$  and  $B$ . Here it is important to note that method II (see Section 2.5) tends to make the dependencies less apparent than when using the average fit, which means that a weak relationship might exist.

Last, we study the effect of the IMF orientation on the BS. The IMF orientation was previously shown to mostly induce asymmetries in the BS shape (Russell et al. 1988; Chai et al. 2015). Thus, we transform the crossings into the aberrated Venus Solar Electric (VSE) coordinates, where  $X_{\text{VSE}}$  stays antiparallel to the average solar wind flow direction (identical to  $X'$ ),  $Y_{\text{VSE}}$  is aligned with the IMF component projected into the VSO  $Y'-Z'$  plane  $\vec{B}_{Y'Z'}$ , and  $Z_{\text{VSE}}$  points in the direction of the solar wind convection electric field  $\vec{E} = -\vec{v}_{\text{SW}} \times \vec{B}_{Y'Z'}$ . The clock angle  $\theta_{\text{VSE}}$  is then defined as the angle between the projection of the spacecraft position in the  $Y_{\text{VSE}}-Z_{\text{VSE}}$  plane and  $Y'_{\text{VSE}}$ .  $\theta_{\text{VSE}} = 0^\circ, 90^\circ, 180^\circ,$  and  $-90^\circ$  mean that the spacecraft is over the magnetic dawn (+B), north (+E), dusk (-B), and south (-E), respectively.

The IMF orientation is linked to the geometry of the shock ( $q_{\parallel}$  and  $q_{\perp}$ ) by the relation

$$\cos(\theta_{\text{Bn}}) = |y \times \cos(\varphi) + z \times \cos(\theta_{\text{VSE}})|, \quad (2)$$

where  $y$  and  $z$  are the lengths of the semi-axes along the  $Y_{\text{VSE}}$ - and  $Z_{\text{VSE}}$ -directions, respectively. A  $q_{\parallel}$  shock is limited by  $|y| \leq 1$  and  $0 \leq z \leq 1$ , which means that there can be no  $q_{\parallel}$  shock crossings over the magnetic poles for high cone angles. As the BS is also farther from the planet at high cone angles and for  $q_{\perp}$  crossings, the  $q_{\parallel}$  crossings are here excluded to avoid orbital bias.

First, we focus on uncovering the magnetic north/south asymmetry. To this extent, we observe the dependence of the BS radius at the terminator with the clock angle, employing method I (see Section 2.5) with 10 bins: five bins for each magnetic hemisphere. The distance at north and south is on average  $2.17 \pm 0.04 R_V$  and  $2.10 \pm 0.04 R_V$  at solar maximum and  $2.27 \pm 0.04 R_V$  and  $2.22 \pm 0.04 R_V$  at solar minimum (Figure 6(a)). The BS is located closer to the planet over



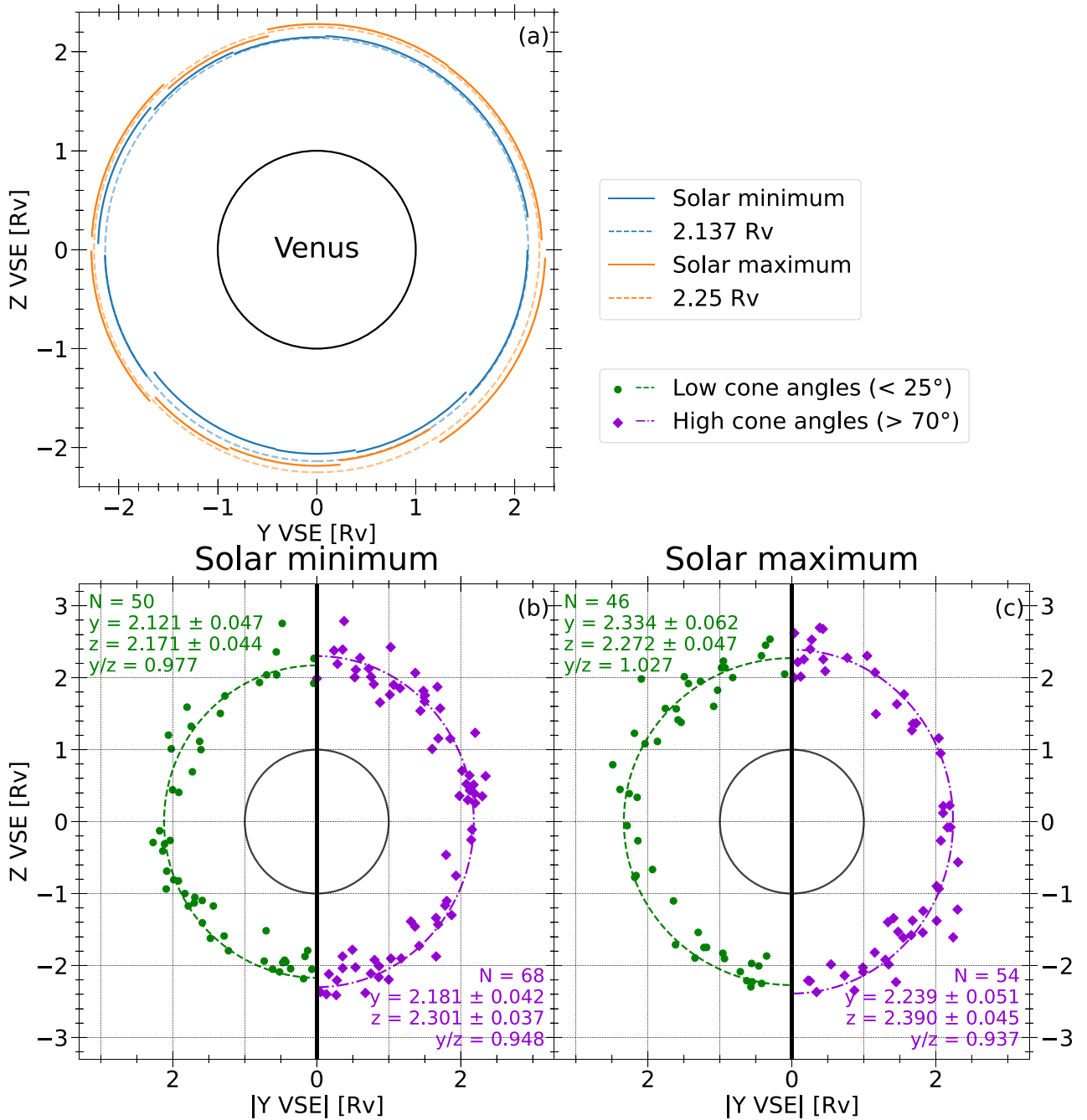


**Figure 6.** BS cross section at the terminator dependence on the direction of the IMF. All plots are shown in VSE ( $Y, Z$ ) [Rv] coordinates, where the  $Y$ -axis is in the direction of the IMF, and the  $Z$ -axis is in the direction of the solar wind convective electric field, both perpendicular to the solar wind flow. (a) Dependence on  $\theta_{\text{VSE}}$  at solar minimum (blue arcs) and solar maximum (orange arcs), revealing the magnetic north/south asymmetry of the BS cross section. The solid arcs are the fitted  $R_T$  values for each  $\theta_{\text{VSE}}$  bin, and the dashed circles represent the mean radius at the terminator values, indicated in the legend. (b) and (c) Dependence on the IMF cone angle, illustrating the magnetic pole-equator asymmetry of the BS cross section in the terminator plane at (b) solar minimum and (c) solar maximum. All BS crossings are extrapolated to the terminator plane (see Section 2.5). BS crossings for low cone angles (green dots,  $< 25^\circ$ ) and high cone angles (violet diamonds,  $> 70^\circ$ ) are fitted by an ellipse. For clarity, the crossings are here shown with an absolute value of  $Y$  VSE, with crossings at low cone angles to the left, and at high cone angles to the right. The number of crossings  $N$  and the semi-axis  $y$  and  $z$  values are indicated in green (upper left) for low cone angles and violet (lower right) for high cone angles. The center black circle in all panels represents Venus.

magnetic south ( $-E$  hemisphere) compared to over magnetic north ( $+E$  hemisphere).

To investigate the magnetic pole/equator asymmetry, we adapt the method developed by Russell et al. (1988). As no asymmetry is detected when we employed the previous method (not shown), we here split our data between high-cone-angle ( $> 75^\circ$ ) and low-cone-angle ( $< 25^\circ$ ) crossings. Within each category, the crossings are then extrapolated to the ( $Y_{\text{VSE}}$ ,

$Z_{\text{VSE}}$ ) terminator plane (see Section 2.5), and the resulting data points are fitted to an ellipse, defined by its semi-axes  $y$  and  $z$ . The cone angle dependency of the magnetic pole/equator asymmetry is clearly visible from Figures 6(b)–(c): the BS is more expanded over the magnetic poles for high cone angles over the full solar cycle, while for low cone angles, the dependence shifts from polar expansion at solar minimum to equatorial expansion at solar maximum. It is interesting to note

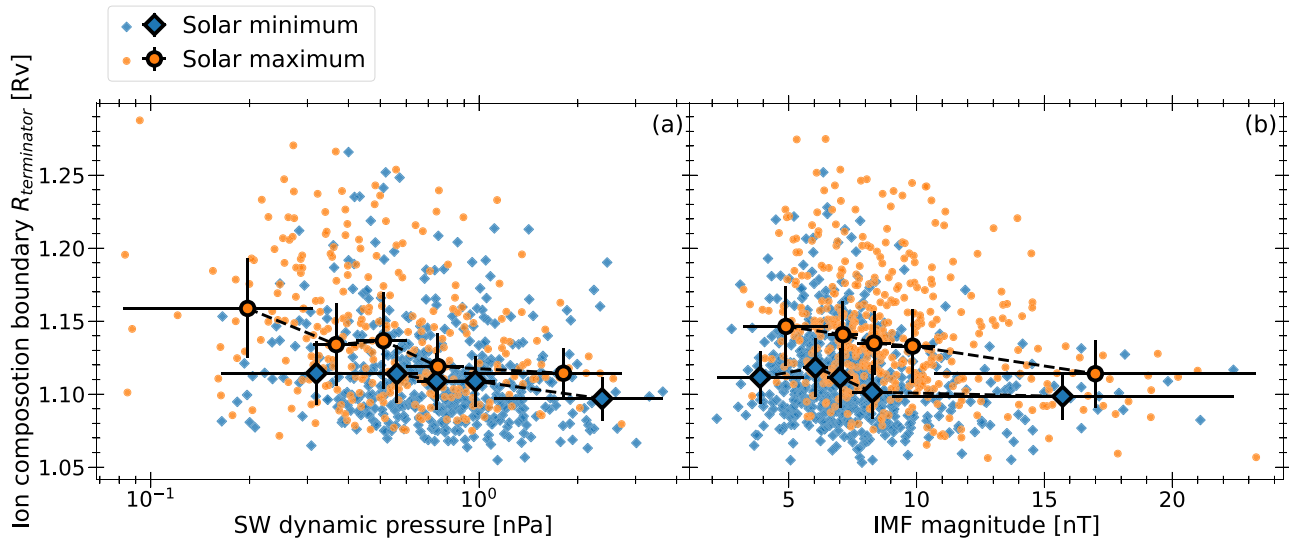


**Figure 7.** ICB radius at the terminator and its dependence on upstream parameters. The blue diamonds (orange dots) represent ICB dayside crossings at solar minimum (maximum). The connected blue diamonds (solar minimum) and orange circles (solar maximum) are the median values over each (a) solar wind dynamic pressure or (b) IMF magnitude bin. The vertical error bars show the median absolute deviation, and the horizontal ones show the widths of the bins.

that when all crossings are considered, the cross section of the BS is roughly circular, which supports the choice of a cylindrical symmetry for fitting the average boundary location.

### 3.2. ICB Dependencies

The evolution of the dayside ICB with upstream parameters is summarized in Figure 7. We find that the size of the dayside ICB is negatively correlated to the solar wind dynamic pressure (Figure 7(a)) and to the IMF magnitude at solar maximum (Figure 7(b)). Moreover, a look at the individual crossings shows that the boundary is less variable for higher values of the upstream parameters, as well as at solar minimum, which suggests that the ICB reaches its minimum altitude under these conditions.

## 4. Discussion

Based on over 5000 independent crossings from more than 8 yr of VEX observations, we carried out an investigation of the solar cycle, solar wind, and IMF control of the Venusian BS location. We corroborate that the position of the BS is mostly sensitive to the solar cycle variations and the IMF magnitude. The solar cycle can be derived from the SSNs, which have a strong correlation with the solar EUV flux (e.g., Russell et al. 1988). The sensitivity to the solar cycle agrees well with earlier studies; Figure 8 shows a comparison of the SSNs and the fitted BS radius at the terminator for VEX (6 months intervals), Venera 9/10 (Smirnov et al. 1980), and PVO (Russell et al. 1988). The correlation between the BS radius and the SSN was explained by the effect of the EUV flux on the neutral atmospheric scale height and the mass loading of the magnetosheath (Alexander & Russell, 1985; Russell et al. 1988; Phillips & McComas 1991; Shan et al. 2015). This discussion is further strengthened by the continued agreement found here for the VEX measurements. In addition, the larger BS radius at the terminator found at solar maximum by PVO, compared to that of VEX, may here be explained by the stronger solar maximum present during the PVO era.

We found different solar wind dynamic pressure effects on the BS shape during solar minimum and maximum. During

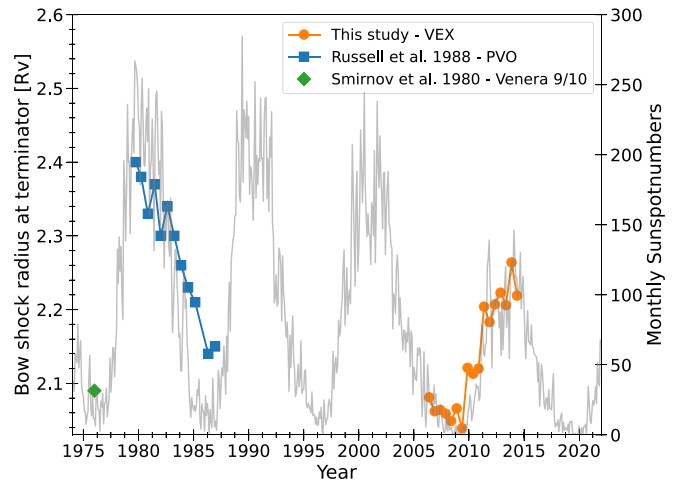


**Figure 8.** Comparison of the BS radius at the terminator found from studies using VEX (orange dots; this study), PVO (blue squares; Russell et al. 1988), and Venera 9/10 (green diamond; Smirnov et al. 1980). The gray line shows the monthly average SSNs, a proxy for the solar cycle.

solar minimum, the effect is minimal, which agrees with previous studies by Russell et al. (1988), Martinecz et al. (2008), Shan et al. (2015), and Chai et al. (2014). However, during solar maximum conditions, the boundary is found to move closer to the planet as the dynamic pressure increases. Measurements from PVO could only find a weak trend on the dynamic pressure for high EUV fluxes. One reason for the difference may lie in the difference of the methods used: with a lot of crossing data at our disposal, we could fit them to a conic shape before estimating the radius at the terminator value (method I; see Section 2.5), while the previous studies used an extrapolation to the terminator plane (method II; see Section 2.5). As stated above, the latter method tends to be less precise than the former method, with less pronounced trends. In addition, one might note that Russell et al. (1988) concluded that the solar wind seemed to exert its control on the BS position mainly through variations of the magnetosonic Mach number and not the dynamic pressure. This trend was attributed by Russell et al. (1988) to the increased flaring of the

BS during lower magnetosonic Mach numbers and therefore an increase in the height at the terminator. Additionally, Tatrallyay et al. (1983) argued that the Alfvén Mach number exerts a strong control on the BS shape and showed that at  $M_A < 4$ , the BS had an extreme increase in terminator distance for a few PVO orbits, while at  $M_A > 7$ , the trend was almost constant. Here, we found that the Alfvén Mach number generally has a negative trend on the BS distance at the terminator. We also note, in agreement with Tatrallyay et al. (1983), that the trend is stronger at  $M_A < 5$ , particularly for solar minimum conditions. In this study, we have opted for the Alfvén Mach number, as the ion and electron temperatures are needed to calculate the magnetosonic Mach number. There is currently no publicly available data set for the two, and the computation of them would require a significant effort, and is thus left for a future study. The difference between the magnetosonic and Alfvén Mach numbers lies in the inclusion of the sonic speed in the denominator of the magnetosonic Mach number equation. This makes the Alfvén Mach number less dependent on the solar wind variations than the magnetosonic Mach number, and more dependent on the IMF magnitude.

We also performed a study of the asymmetries of the BS shape in the terminator region, using only the quasi-perpendicular BS crossings, where we found two different types of asymmetries. First, there is a north–south asymmetry, where the BS is located at a higher altitude over the magnetic north than the magnetic south, i.e., in the direction of the solar wind convection electric field. This trend agrees with previous studies on PVO measurements (e.g., Alexander et al. 1986; Phillips et al. 1986; Russell et al. 1988) and VEX measurements during solar minimum (Chai et al. 2014, 2015). Notably, the magnetic field measurements by PVO also showed that there is an asymmetry in the magnetic field draping patterns in the magnetosheath (Phillips et al. 1986). The asymmetries of both the BS position and the magnetic field draping pattern are attributed to the mass loading due to the ion pickup process, as the efficiency of the ion pickup is the largest where the convective electric field points away from the planet, i.e., the magnetic north (Alexander et al. 1986; Russell et al. 1988).

Second, there is a magnetic pole–equator asymmetry, which changes with the cone angle. For high cone angles, the BS is generally located at a higher altitude near the magnetic poles compared to the magnetic equator, for both solar minimum and solar maximum conditions. During high cone angles, the IMF and solar wind flow direction is almost perpendicular, which provides a strong convective electric field. Therefore, as with the magnetic north–south asymmetry, the asymmetry is likely related to the mass loading of the solar wind by the pickup ion process (Alexander et al. 1986). However, for low cone angles, when the IMF is almost aligned with the solar wind flow direction and the solar wind electric field is weak, the BS is found to be located at a higher altitude in the magnetic equator, which is an opposite trend compared to the high cone angles. However, this asymmetry is only apparent during solar maximum conditions, as the cross section is almost circular or even has an opposite asymmetry during solar minimum and low cone angles.

Our investigation of the ICB has shown that its size has small variations with respect to the upstream solar wind dynamic pressure, with a slightly stronger response during solar maximum. This is similar to the response by the BS, which points to shared underlying physical mechanisms. The

size of the ICB is mainly related to the pressure balance between the thermal pressure of the ionosphere, which increases with a higher EUV radiation flux, and the dynamic pressure of the solar wind. As expected, the size of the ICB generally increased during solar maximum compared to minimum when we constrained the dynamic pressure (Figure 7(a)) and generally decreased during higher dynamic pressures when we constrained the solar activity. However, the trends are less pronounced, or almost negligible, for the solar minimum conditions. Similarly, the magnitude of the IMF has a strong effect on the ICB during solar maximum, but is negligible during solar minimum conditions (Figure 7(b)). These results could be connected to the magnetic state changes of the Venusian ionosphere, where during the magnetized state the IMF penetrates into the ionosphere and aids in the pressure balance between the ionosphere and the solar wind (Luhmann & Cravens 1991; Angsmann et al. 2011). The magnetized state occurs preferentially during times when the ionospheric thermal pressure is low, such as during solar minimum conditions when the solar EUV radiation flux is low, and when the dynamic pressure is high. This leads to a situation where the dynamic pressure of the solar wind, and the magnetic pressure of the magnetic pileup boundary (Zhang et al. 1991), overwhelm the thermal pressure of the ionosphere, which thus changes from an unmagnetized to a magnetized state (Luhmann & Cravens 1991; Angsmann et al. 2011). If the ionosphere is in a magnetized state, the ionospheric pressure will also include part of the (originally) external pressure exerted by the IMF, which may help maintain the boundary altitude during higher dynamic pressures. Therefore, if the ionosphere transitions to a magnetized state, it may counteract the lowering of the altitude at an increased dynamic pressure, which normally occurs when the ionosphere is “stronger” during solar maximum conditions. The magnetic state of the ionosphere during the time of the identified boundary crossings used in this study has not been investigated here, and provides an interesting direction for a future study.

## 5. Conclusions

In summary, we have derived the average BS position and shape during the full VEX era. We have provided the average models for both solar minimum and solar maximum conditions. By investigating the relationship with upstream conditions, we have also shown that the BS terminator radius:

1. increases from solar minimum to solar maximum conditions;
2. decreases during higher-solar-wind dynamic pressures at solar maximum, but remains constant at solar minimum;
3. increases when the IMF magnitude increases; and
4. decreases with an increase in the Alfvén Mach number.

These results point toward the strong control of the Venusian boundaries by the solar cycle, mainly through the solar EUV radiation flux, presumably, which affects the neutral atmospheric scale height and the mass loading of the magnetosheath, as well as the subsequent expansion of the Venusian induced magnetosphere and BS size. The mass loading by planetary pickup ions in the magnetosheath can here also explain the observed asymmetry of the BS in the terminator plane, where in the VSE coordinate system we found that there is

1. a magnetic north–south asymmetry, with a larger distance from the planet in the direction of the solar wind convective electric field; and
2. a magnetic pole–equator asymmetry, with a larger distance from the planet near the poles compared to the equator for high cone angles, an opposite trend for low cone angles at solar maximum conditions, and no asymmetry for low cone angles at solar minimum conditions.

Finally, for the ICB, we have shown that its terminator distance from the planet

1. decreases with an increase in the solar wind dynamic pressure, with a more pronounced trend during solar maximum conditions compared to solar minimum; and
2. decreases for increased IMF magnitudes, which is also more pronounced during solar maximum conditions.

These results suggest that the pressure balance at the ICB between the solar wind dynamic pressure, the magnetic pressure, and the ionospheric thermal pressure plays a strong role during solar maximum conditions. The lack of strong trends during solar minimum may indicate that the change of magnetization state of the ionosphere is important during solar minimum conditions.

### Acknowledgments

We acknowledge the European Space Agency (ESA) for supporting the successful Venus Express mission. M.P. acknowledges funding from the European Union’s Horizon 2020 program under grant agreement No. 871149 for Europlanet 2024 RI. M.P. and S.B. acknowledge funding from the Japan Society for the Promotion of Science (postdoctoral fellowships for research in Japan). The ASPERA-4 and MAG data used in this study are publicly available via the ESA Planetary Science Archive (PSA; <https://www.cosmos.esa.int/web/psa/Venus-express>). The data may also be acquired at AMDA (<http://amda.irap.omp.eu/>), provided by the Centre de Données de la Physique des Plasmas (CDPP) and supported by CNRS, CNES, and Observatoire de Paris and Université Paul Sabatier, Toulouse. The sunspot number data were downloaded from <https://www.sidc.be/silso/datafiles>. The identified bow shock and ion composition boundary crossings used in this study are publicly available at doi:10.5281/zenodo.7679678 (Persson et al. 2023).

### ORCID iDs

M. Persson  <https://orcid.org/0000-0003-3497-3209>  
 Y. Futaana  <https://orcid.org/0000-0002-7056-3517>

S. Aizawa  <https://orcid.org/0000-0002-3483-3444>  
 N. André  <https://orcid.org/0000-0001-8017-5676>  
 S. Bergman  <https://orcid.org/0000-0003-0673-2264>  
 A. Fedorov  <https://orcid.org/0000-0002-9975-0148>  
 C. Mazelle  <https://orcid.org/0000-0001-5332-9561>  
 S. Rojas Mata  <https://orcid.org/0000-0003-3602-156X>

### References

- Alexander, C. J., & Russell, C. T. 1985, *GeoRL*, **12**, 369  
 Alexander, C. J., Luhmann, J. G., & Russell, C. T. 1986, *GeoRL*, **13**, 917  
 Angsmann, A., Fränz, M., & Dubinin, E. 2011, *P&SS*, **59**, 327  
 Barabash, S., Sauvaud, J. A., Gunell, H., et al. 2007, *P&SS*, **55**, 1772  
 Chai, L., Wan, W., Fraenz, M., et al. 2015, *JGRA*, **120**, 4446  
 Chai, L. M., Fraenz, W., Wan, Z., et al. 2014, *JGRA*, **119**, 9464  
 Colin, L. 1980, *JGR*, **85**, 7575  
 Fedorov, A., Barabash, S., & Sauvaud, J. A. 2011, *JGR*, **116**, A07220  
 Futaana, Y., Stenberger Wieser, G., Barabash, S., & Luhmann, J. G. 2017, *SSRv*, **212**, 1453  
 Hall, B. E. S., Sánchez-Cano, B., Wild, J. A., Lester, M., & Holmstrom, M. 2019, *JGRA*, **124**, 4761  
 Hobara, Y., Balikhin, M., Krasnoselskikh, V., Gedalin, M., & Yamagishi, H. 2010, *JGRA*, **115**, A11106  
 Holmberg, M. K. G., André, N., Garnier, P., et al. 2019, *JGRA*, **124**, 8564  
 Luhmann, J. G., & Cravens, T. E. 1991, *SSRv*, **55**, 201  
 Martinecz, C., Boeswetter, A., Fränz, M., et al. 2009, *JGRE*, **114**, E00B30  
 Martinecz, C., Fränz, M., Woch, J., et al. 2008, *P&SS*, **56**, 780  
 Newbury, J. A., Russell, C. T., & Gedalin, M. 1998, *JGRA*, **103**, 29581  
 Persson, M., Bergman, S., Signoles, C., et al. 2023, Venusian bow shock crossings manually identified from measurements by the ASPERA-4 and MAG instruments onboard Venus Express, Zenodo, doi:10.5281/zenodo.7679677  
 Persson, M., Futaana, Y., Ramstad, R., et al. 2021, *GeoRL*, **48**, e91213  
 Phillips, J. L., Luhmann, J. G., Russell, C. T., et al. 1986, *Adv. Space. Res.*, **6**, 179  
 Phillips, J. L., & McComas, D. J. 1991, *SSRv*, **55**, 1  
 Ramstad, R., Barabash, S., Futaana, Y., Nilsson, H., & Holmström, M. 2017b, *JGRA*, **122**, 8051  
 Ramstad, R., Barabash, S., Yoshifumi, F., & Holmström, M. 2017a, *JGRA*, **122**, 7279  
 Rong, Z. J., Barabash, S., & Futaana, Y. 2014, *JGRA*, **119**, 8838  
 Russell, C. T. 1992, in *Venus and Mars: Atmospheres, Ionospheres, and Solar Wind Interactions*, ed. J. G. Luhmann, M. Tatrallyay, & R. O. Pepin (Washington, D.C.: American Geophysical Union), 225  
 Russell, C. T., Chou, E., & Luhmann, J. G. 1988, *JGR*, **93**, 5461  
 Russell, C. T., Luhmann, J. G., & Strangeway, R. J. 2006, *P&SS*, **54**, 1482  
 Shan, L., Quanming, Lu., Christian, M., et al. 2015, *P&SS*, **109**, 32  
 Slavin, J. A., Elphic, R. C., Russell, C. T., et al. 1980, *JGR*, **85**, 7625  
 Svedhem, H., Titov, D. V., McCoy, D., et al. 2007, *P&SS*, **55**, 1636  
 Smirnov, V. N., Vaisberg, O. L., & Intriligator, D. S. 1980, *JGR*, **85**, 7651  
 Tatrallyay, M., Russell, C. T., Mihalov, J. D., & Barnes, A. 1983, *JGRA*, **88**, 5613  
 Zhang, T. L., Berghofer, G., Magnes, W., et al. 2007, ESA Special Publication SP 1295 (Paris: ESA)  
 Zhang, T. L., Delva, M., Baumjohann, W., et al. 2008, *P&SS*, **56**, 785  
 Zhang, T.-L., Luhmann, J. G., & Russell, C. T. 1990, *JGR*, **95**, 14961  
 Zhang, T. L., Luhmann, J. G., & Russell, C. T. 1991, *JGR*, **96**, 11145